Materials & Design 225 (2023) 111473

Contents lists available at ScienceDirect

Materials & Design

journal homepage: www.elsevier.com/locate/matdes

Superior fracture toughness with high yield strength in a high-Mn steel induced by heterogeneous grain structure

Shengde Zhang [a,b], Muxin Yang [a], Xiaolei Wu [a,b], Fuping Yuan [a,b,*]

[a] State Key Laboratory of Nonlinear Mechanics, Institute of Mechanics, Chinese Academy of Sciences, Beijing 100190, People's Republic of China
[b] School of Engineering Science, University of Chinese Academy of Sciences, Beijing 100190, People's Republic of China

HIGHLIGHTS

- A heterogeneous grain structure was designed in a high-Mn steel to obtain excellent synergy of fracture toughness and strength.
- Heterogeneous grain structures induce larger size of plastic zone and higher strain hardening capacity around crack tips.
- Grain refinement and high density of geometrically necessary dislocations were observed along crack paths in heterogeneous structures for high toughness.
- The observed higher fracture toughness in heterogeneous grain structures can be partly attributed to formation of microbands.

GRAPHICAL ABSTRACT

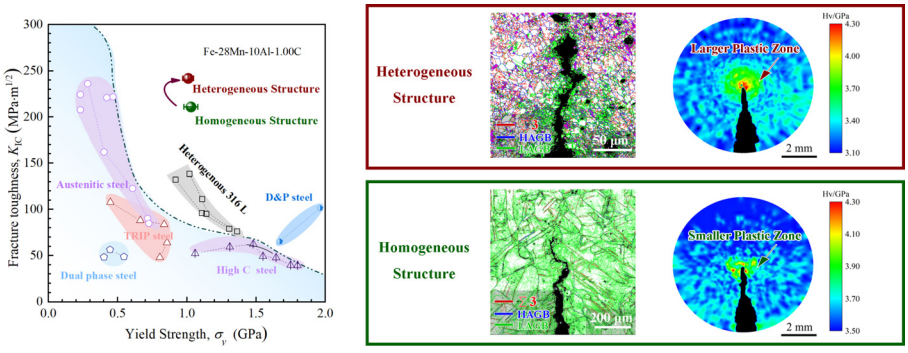

ARTICLE INFO

Article history:
Received 13 September 2022
Revised 5 December 2022
Accepted 6 December 2022
Available online 7 December 2022

Keywords:
Heterogeneous grain structures
Fracture toughness
Strain hardening, Microband-induced plasticity
Ductility
Mn austenitic steels

ABSTRACT

Heterogeneous grain structures were designed in a high Mn steel (Fe28Mn10Al1.00C), and the tensile properties and fracture toughness were investigated and compared with those for homogeneous structures. The heterogeneous grain structures display larger tensile ductility, stronger strain hardening and higher fracture toughness at the similar yield strength level. Hetero-deformation-induced hardening is found to play an important role in the heterogeneous grain structures, resulting in better mechanical properties. The size of plastic zone and the strain hardening capacity around the crack tip for the heterogeneous grain structures are found to be much larger/higher than those for the homogeneous grain structures at the same level of yield strength, resulting in better fracture toughness. High density of geometrically necessary dislocations and grain refinement are induced at the adjacent area of the main crack path, and numerous microvoids are also observed besides the main crack for the heterogeneous grain structures, resulting in more energy dissipation for higher fracture toughness. The deformation mechanisms around the crack tip are highly dependent on the magnitude of plastic strain and the grain size. The observed higher fracture toughness in the heterogeneous grain structures can be partly attributed to the formation of microbands.

1. Introduction

High strength and excellent ductility/toughness are always demanded in steels for practical applications [1–10]. Through several generations of development, advanced steels, such as

* Corresponding author at: State Key Laboratory of Nonlinear Mechanics, Institute of Mechanics, Chinese Academy of Sciences, Beijing 100190, People's Republic of China.
E-mail addresses: zhangshengde@imech.ac.cn (S. Zhang), mxyang@lnm.imech.ac.cn (M. Yang), xlwu@imech.ac.cn (X. Wu), fpyuan@lnm.imech.ac.cn (F. Yuan).

https://doi.org/10.1016/j.matdes.2022.111473
0264-1275/

twinning-induced plasticity steels (TWIP) [11,12], dual-phase steels [13,14] and transformation-induced plasticity (TRIP) steels [15,16], have attracted extensive research interests in last two decades. In the automotive industry, the absorbed energy under tensile loading, i.e., the product of tensile strength and total elongation, is generally considered as a judgement for the mechanical properties of steels, the steels with a product of about or over 50000 MPa% can be called the advanced steels [3,4,11,15]. The strength and ductility in steels can be tailored in general by the grain size, the constituent phases and the chemical composition [2,4,11].

Among the advanced steels, the Mn austenitic steels have attracted extensive research efforts due to their excellent mechanical properties [1,3,4,6,8,11–16]. With increasing Mn content and stacking faulting energy (SFE), the dominant deformation mechanism is transited from TRIP effect to TWIP effect in the Mn austenitic steels [11–14]. These two effects have been considered as two promising deformation mechanisms due to the extraordinary strain hardening ability induced by martensite transformation and so called "dynamic Hall-Petch effect". Since higher standard for safety and reduced weight are demanded for automotive industries in the future, more advanced steels with better mechanical properties and lower density should be designed. In last decade, a novel high-Mn steel with high SFE (50–90 mJ m^{-2}), called as the microband-induced plasticity (MBIP) steel [17–27], has been developed. Moreover, an excellent synergy of strength/ductility can also be achieved in high entropy alloys due to TRIP effect, TWIP effect or MBIP effect with regulating SFE [28,29]. In the MBIP steels, significant weight reduction and better tensile properties (a product of tensile strength and total elongation of about 90000 MPa %) can be achieved by ~10 wt% Al addition into the high Mn steels with about 28–30 wt% Mn. The generations of microbands and highly dense dislocation walls in the grain interiors by geometrically necessary dislocations (GNDs) were found to play an important role on the strain hardening of MBIP steels.

The practical applications of the Mn austenitic steels with coarse grains (CGs) are restricted and limited by their low yielding strength. The Mn austenitic steels can generally be strengthened by grain refinement or cold working, while such elevation in strength results in a remarkable loss of ductility [3,5,9,10,18,25]. Heterogeneous grain structures have been proven to be a promising strategy to obtain superior synergy of strength and ductility in metals and alloys [29–32]. The excellent tensile properties for heterogeneous grain structures can be attributed to the strain partitioning between grains with various grain sizes, the GNDs at domain boundaries and the hetero-deformation-induced (HDI) hardening [33]. Thus, the strategy of heterogeneous grain structures can be utilized in the MBIP steels to achieve better mechanical properties.

Besides yield strength and uniform elongation during tensile loading, the damage tolerance, such as fracture toughness, should also be considered for practical structural applications [34–44]. In general, fracture toughness and strength are mutually exclusive in homogeneous structures since the fracture toughness is determined by the energy absorption ability during the process of crack nucleation and propagation [36]. The energy absorption during initiation is generally related to the intrinsic toughening mechanisms, which are associated with the hardening capacity and the size of plastic zone around cracks. While, the energy absorption during propagation is controlled by the extrinsic toughening mechanisms, such as crack shielding and crack bridging [36]. Thus, heterogeneous grain structures should also have potential to achieve both high strength and excellent fracture toughness, resolving the toughness-strength dilemma [41–44], since extra HDI hardening can be obtained in heterogeneous grain structures due to GNDs generated at domain boundaries and strain partitioning between varying domains [33]. However, the toughening mechanisms in the MBIP steels with heterogeneous grain structures are still unclear, and how heterogeneous grain structures affect the initiation and propagation of cracks should be clarified. In these regards, heterogeneous grain structures were designed and fabricated in a high Mn MBIP steel, and the fracture behaviors and the corresponding toughening mechanisms were systematically studied.

2. Materials and experimental procedures

The chemical content for the high Mn MBIP steel is as following: 27.9Mn, 9.8Al, 1.02C, 0.002Si, 0.003S, 0.01P, 0.002O, with balance of Fe (wt. %). The high Mn MBIP steel was fabricated by repeated melting under Ar atmosphere and cast into rods with 30 mm diameter. The cast rods were then forged into rods with 22 mm diameter at 900 °C. The rods were then homogenized at 1200 °C for 2 h followed by water quenching to obtain a CG structure with single austenitic phase (named as the CG sample). The homogenized rods were first deformed by equal-channel angular pressing (ECAP) for one pass, and then the ECAPed rods were further deformed by cold rolling (CR) with a thickness reduction of about 42 % (named as the ECAP + CR sample). According to the previous research [22], the ECAP + CR samples were then annealed at 890 °C for 5 min to obtain heterogeneous grain structures (named as the HS sample) with a single austenite phase. Homogeneous structures with a similar yield strength to the HS sample were also fabricated by only cold rolling with a smaller thickness reduction of about 25 % based on the CG sample (named as the CR sample). Thus, the tensile and fracture behaviors of the HS sample and the CR sample were investigated and compared.

All quasi-static uni-axial tensile tests and load-unload-reload (LUR) tests were conducted by an MTS landmark machine at room temperature and at a strain rate of 5×10^{-4} s^{-1}, utilizing a dog-bone shaped sample with gauge dimensions of $10 \times 2.5 \times 1.0$ m m^3. The tensile direction was along the rolling direction. Miniaturized compact tension specimens were utilized for the fracture toughness tests, and the crack propagation direction was set to be perpendicular to the rolling direction. The fracture toughness tests were conducted and the load-line displacement curves were obtained using an MTS landmark machine. The dimensions of the miniaturized compact tension specimens are as follows: a width of 12 mm (W), a thickness of 6 mm (B), and an initial notch length of about 5.4 mm (a_0). Sharp fatigue crack tip was then produced under a tension–tension loading mode until reaching a total crack length of about 6 mm. Side grooves on both surfaces with a depth of about 0.1B were machined in order to obtain valid data and avoid obvious crack tunneling. Side grooves generally can insure the straight crack extension by enhancing the surface stress constraint. The crack mouse opening displacements (CMOD) were measured by a contactless video crack opening displacement gauging (VCOD) system. The details for the VCOD gauging system and the determination method for the instantaneous crack length from CMOD by the unloading compliance technique can be found in the previous paper [44]. The J-R curves were then calculated according to the ASTM standard E1820 [45].

The microstructures before and after fracture toughness tests were characterized and revealed by Electron backscattered diffraction (EBSD) and transmission electron microscope (TEM). The fracture surfaces were revealed by scanning electron microscope (SEM). The strain hardening capacity around the crack tip was characterized by micro-hardness measurements utilizing a Vickers diamond indenter with 25 g load and 15 s dwell time. The other details for microstructure characterization can be referred to our previous paper [44].

3. Results and discussions

The EBSD images for the CG sample, the HS sample and the CR sample are displayed in Fig. 1. The images for inverse pole figure (IPF) are shown in Fig. 1a1, 1b1 and 1c1, respectively. The phase maps in the insets of Fig. 1a1, 1b1 and 1c1 indicate that these three samples are fully composed of austenite phase. The maps with various boundaries (high-angle grain boundaries, low-angle grain boundaries and twin boundaries) for these three samples are displayed in Fig. 1a2, 1b2 and 1c2, respectively. Moreover, the maps of kernel average misorientation (KAM) for the HS sample and the CR sample are shown in Fig. 1b3 and 1c3. The grain size distributions for the CG and the CR sample are displayed in Fig. 1a3. As indicated in Fig. 1a1-1a3, the CG sample has a relatively homogeneous structure with CGs, and the average grain size for the CG sample is about 183 μm. The HS sample has a low KAM value and a low dislocation density due to the annealing at 890 °C for 5 min (Fig. 1b3). The grains in the HS sample are also fully recrystallized (Fig. 1b2 and b3), while the HS sample shows a heterogeneous grain structure, bimodal grain size distribution is observed for the HS sample (one peak at about 1 μm for small grains, and the other peak at about 10 μm for large grains). As indicated in Fig. 1c1, the CR sample shows a relatively homogeneous CG structure, while the CR sample has a high KAM value (Fig. 1c3) due to the small thickness reduction of about 25 % during the CR process. This high KAM value indicates that high density of dislocations were introduced to the CR sample. Moreover, numerous low-angle grain boundaries are observed in the CR sample, and the sub-grain structures are formed due to the high density of dislocations.

TEM observations for the HS sample and the CR sample are shown in Fig. 2. TEM images for the HS sample are displayed in

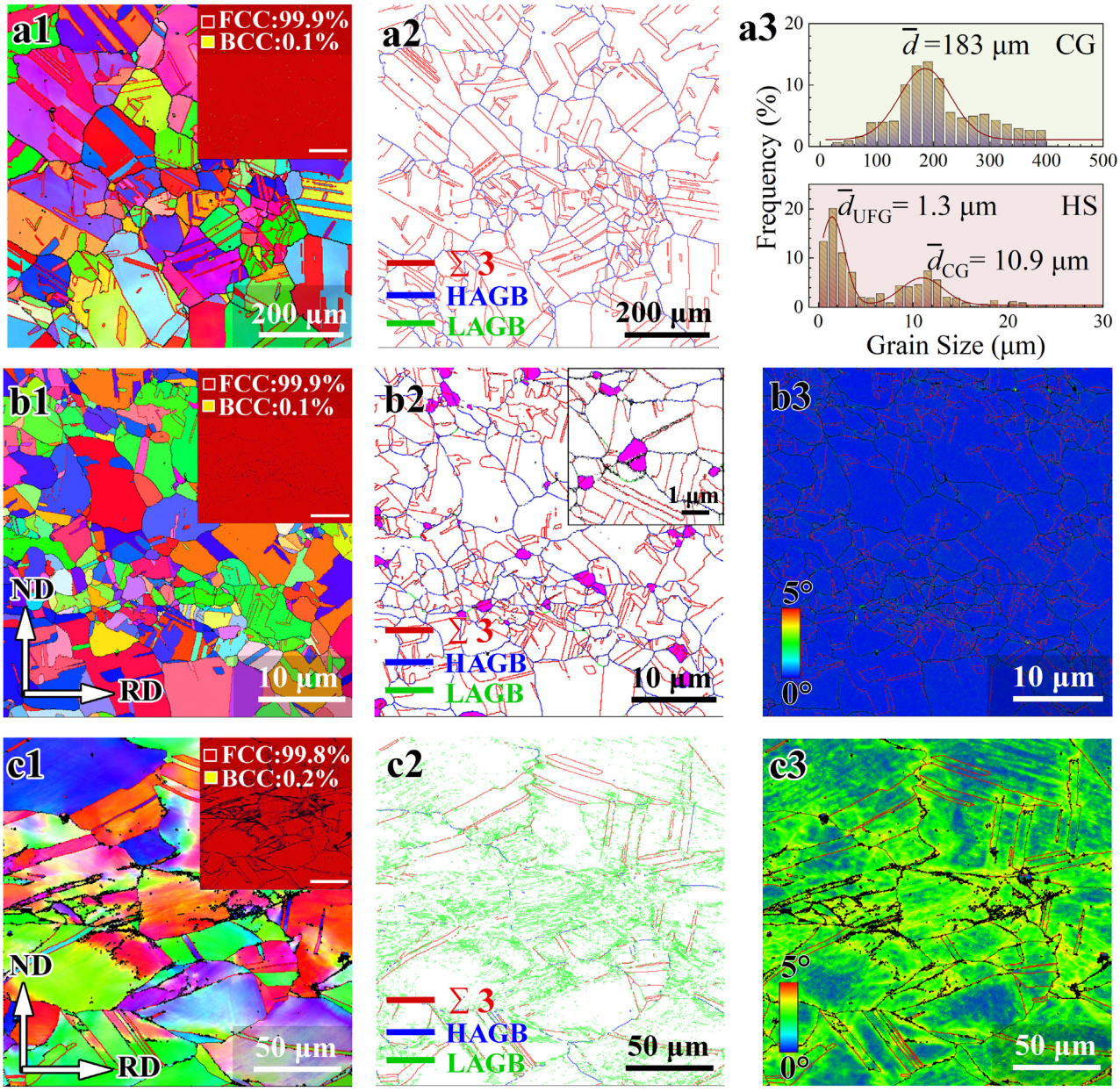

Fig. 1. EBSD images for the CG sample, the HS sample and the CR sample. The IPF images for (a1) the CG sample; (b1) the HS sample and (c1) the CR sample. The corresponding phase maps are also shown in the insets of (a1), (b1) and (c1). The maps with various boundaries for (a2) the CG sample; (b2) the HS sample and (c2) the CR sample. (a3) The grain size distributions for the CG sample and the HS sample. The KAM maps for (b3) the HS sample; (c3) the CR sample.

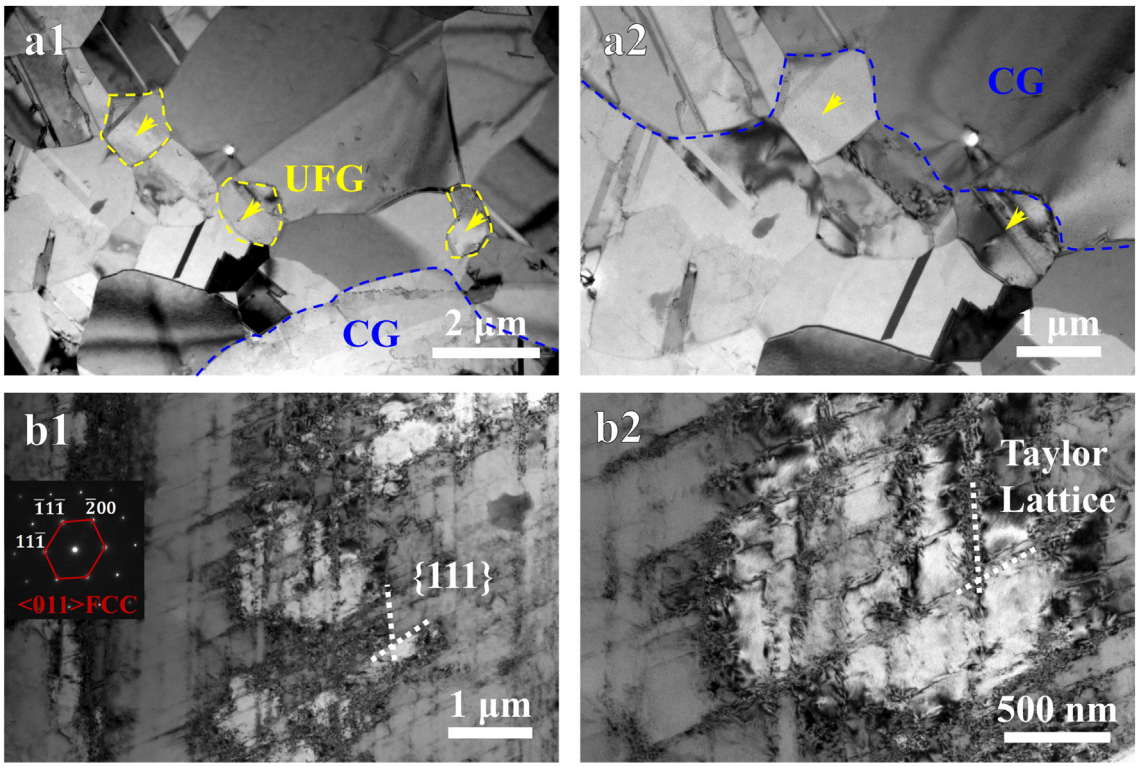

Fig. 2. TEM images for (a1-a2) the HS sample and (b1-b2) the CR sample.

Fig. 2a1 and 2a2, while those for the CR sample are shown in Fig. 2b1 and 2b2. In the HS sample, both large grains with grain size of about several or 10 μm (marked by blue text) and small ultra-fine grains (UFGs) with grain size of about 1 μm or less (marked by yellow text and arrows) can be observed. Straight annealed coherent twin boundaries can also be observed in the HS sample. The dislocation density is very relatively low in the HS sample, especially in the large grains. Due to the large grains, no high-angle grain boundaries are observed in the TEM images for the CR sample, while high density of sub-grain structures can be observed (Fig. 2b1 and 2b2). Planar dislocations on two slip {1 1 1} planes are observed, Taylor lattices with a relatively low energy are formed due to high density of planar dislocations on two slip systems [17]. Small domains can be divided by these Taylor lattices, resulting in strengthening and reduced strain hardening capacity.

Then tensile properties for the typical four samples (CG, ECAP + CR, CR, HS) are displayed in Fig. 3. Fig. 3a and 3b show the engineering stress–strain curves and the curves for the normalized harden rate ($(\partial\sigma/\partial\varepsilon)/\sigma$) as a function of true strain. The CG sample has a low yield strength of 523 MPa, while a uniform elongation as high as 71.5 %. After severe plastic deformation by ECAP and CR, the yield strength is elevated to 1580 MPa, while the uniform elongation is reduced to almost zero. The yield strength is about 1048 MPa, and the uniform elongation is 7.2 % for the CR sample. The HS sample has a similar yield strength (998 MPa) as compared to the CR sample, while the HS sample has a much higher uniform elongation (34.5 %). The total elongations are about 34.9 % and 43.8 % for the CR sample and the HS sample, respectively. Thus, the heterogeneous grain structures show a better synergy of strength and ductility due to the HDI hardening and GNDs induced at domain boundaries [33]. The HS sample also shows a much higher normalized hardening rate as compared to the CR sample, and displays an up-turn phenomenon, which can be attributed to the elastic–plastic transition stage for the heterogeneous grain structures and the strain partitioning between grains with various grain sizes [33]. It is interesting to note that the normalized hardening rate in the HS sample is even higher than that in the CG sample at some strain range. The LUR tests have been conducted on the three samples (the CR sample, the HS sample and the CG sample), the true stress–strain curves for LUR tests on these three samples are shown in Fig. 3c. Based on the method proposed in our previous paper [33], the back stress (σ_{HDI}) can be calculated, and then the back stress (σ_{HDI}) and the fraction of HDI stress on the overall flow stress (σ_{HDI}/σ_f) are plotted as a function of true strain for these three samples. It is clearly indicated that HDI hardening plays a more important role in the HS sample, as compared to the CG sample and the CR sample, resulting in better tensile properties in the HS sample.

The fracture toughness values for the HS sample and the CR sample have been obtained and compared. These two samples have similar yield strength, thus the fracture toughness of heterogeneous grain structure (the HS sample) could be compared to the homogeneous structure (the CR sample) at the similar strength level. The curves of force P vs displacement for these two samples are displayed in Fig. 4a. The maximum force value can be defined as P_{max}, while the force point with a slope equal to 95 % of the initial slope can be denoted as P_Q. Thus obvious plastic deformation around crack tip before crack propagation can be identified since P_{max}/P_Q is larger than 1.1. Since the critical stress-intensity factor K_{IC} is usually defined under the linear-elastic plane strain condition, thus the direct calculations for K_{IC} from these curves are not valid any more. Thus, J-integral method is used to obtain the J_Q since the elastic–plastic conditions are applied for these two samples.

The J-R curves (J-integral vs crack extension $\triangle a$) for these two samples are shown in Fig. 4b. The sample thickness and the initial left crack ligament (W-a_0) were selected to satisfy the plane strain condition based on the ASTM standard E1820 [45]. Moreover, the machined side grooves can guarantee that the cracks propagate

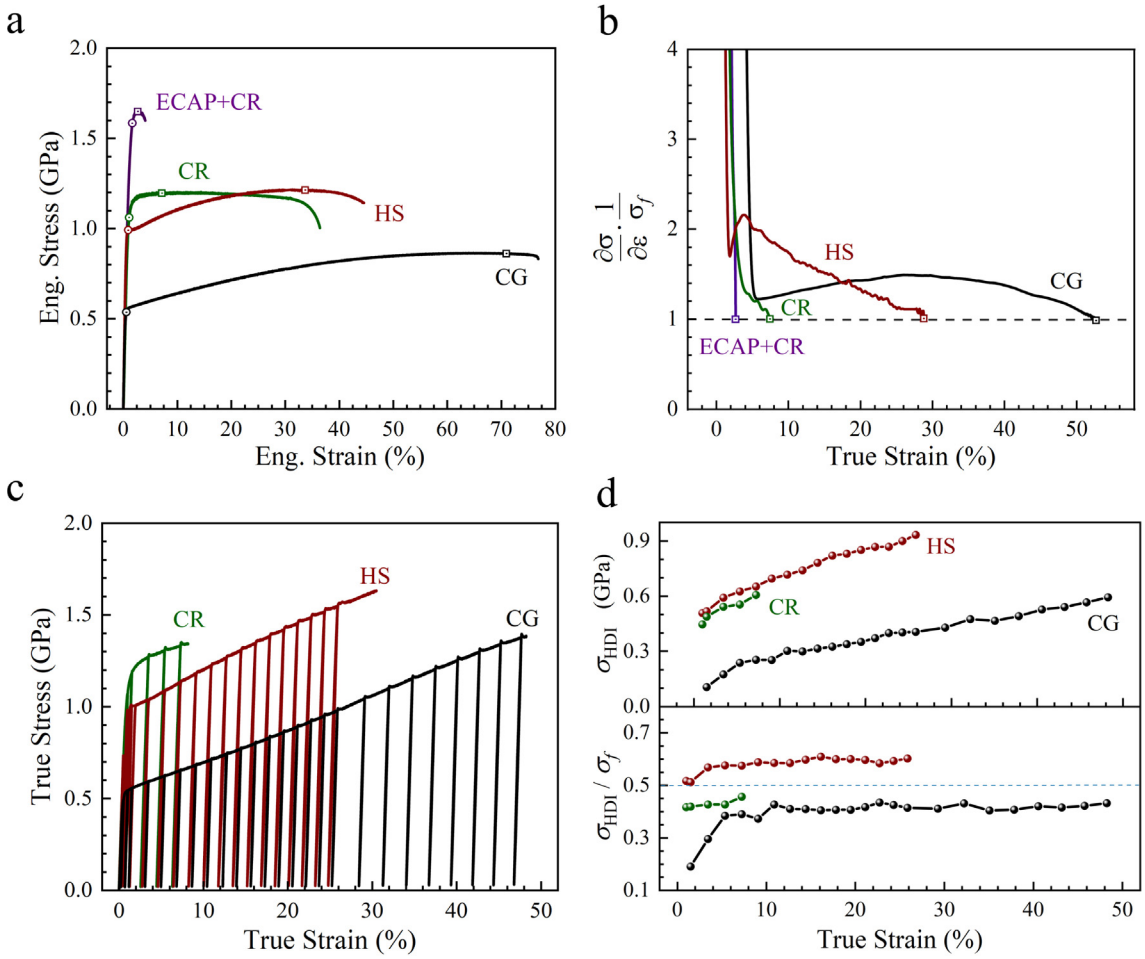

Fig. 3. Tensile properties for the typical four samples (CG, ECAP + CR, CR, HS). (a) Engineering stress–strain curves. (b) Normalized harden rate ($(\partial\sigma/\partial\varepsilon)/\sigma$) vs true strain. (c) True stress–strain curves for LUR tests. (d) Curves of σ_{HDI} and σ_{HDI}/σ_f as a function of true strain.

straightly. Thus, J_Q can be considered as the intrinsic fracture toughness of materials (J_{IC}), and J_{IC} can be determined by the intersections of 0.2 mm offset blunting lines with the *J-R* curves. The values of J_{IC} for the CR sample and the HS sample are calculated to be 193.9 and 254.2 kJ/m^2, respectively. The values of critical stress-intensity factor K_{IC} for these samples can be determined to be 211.5 and 242.2 MPa·m$^{1/2}$, respectively, based on the equation of $K_{IC}=\sqrt{\frac{EJ_{IC}}{1-\nu^2}}$($E$ = 210 GPa is the Young's modulus, ν = 0.3 is the Poisson's ratio). It is clearly indicated that the HS sample has higher fracture toughness, larger tensile uniform elongation, stronger strain hardening at the similar yield strength level, as compared to the CR sample. Thus, the heterogeneous grain structure (the HS sample) is found to have a better synergy of strength and ductility/toughness over the homogeneous structure (the CR sample) in the present MBIP steel. The K_{IC} is plotted as a function of σ_y for the present data in Fig. 4c, along with the data for the other advanced steels [9,41,46–53]. Three repeated tests were conducted for each sample, and the error bars are provided in Fig. 4c. It is also clearly observed that the present MBIP steel has a better synergy of strength and fracture toughness, as compared to the other advanced steels.

The fracture surfaces of the aforementioned two samples after fracture toughness tests are characterized by SEM in Fig. 5 for revealing the toughening mechanisms. These two samples both show typical ductile fracture features. Lots of ductile dimples can be observed for both samples, thus the nucleation and propagation of cracks should be accompanied with initiation and coalescence of microvoids. The dimple size distributions for the HS sample and the CR sample are displayed in Fig. 5a3 and 5b3. It is interesting to note that the dimple size of the CR sample is relatively uniform, while a bimodal dimple size distribution can be observed for the HS sample, which could be attributed to the heterogeneous grain distribution in the HS sample. Thus, the high fracture toughness in these two samples can be attributed to the high density of dimples and the ductile fracture mode.

The fracture toughness of materials is generally dependent on the size of plastic zone and the strain hardening capacity around the crack tip. Thus, the contours for the micro-hardness distributions around the crack tips for the HS sample and the CR samples are displayed and compared in Fig. 6. Based on these two contours, the micro-hardness is averaged at the same distance from the crack tips, and then the average value of micro-hardness is plotted as a function of distance from the crack tips in Fig. 6a2 and 6b2 for the HS sample and the CR sample, respectively. Here, the plastic zone can be defined as the area with obvious higher hardness than that before fracture toughness tests. Based on this definition, the size of plastic zone is estimated to be about 1.7 mm and 1.0 mm for the HS sample and the CR sample, respectively. Moreover, the average hardness increment in the plastic zone is calculated to be about 1.21 GPa and 0.55 GPa for the HS sample and the CR sample, respectively. The average hardness increment in the plastic zone can be considered as an indicator for the strain hardening capacity around the crack tip. It is also well known that the size

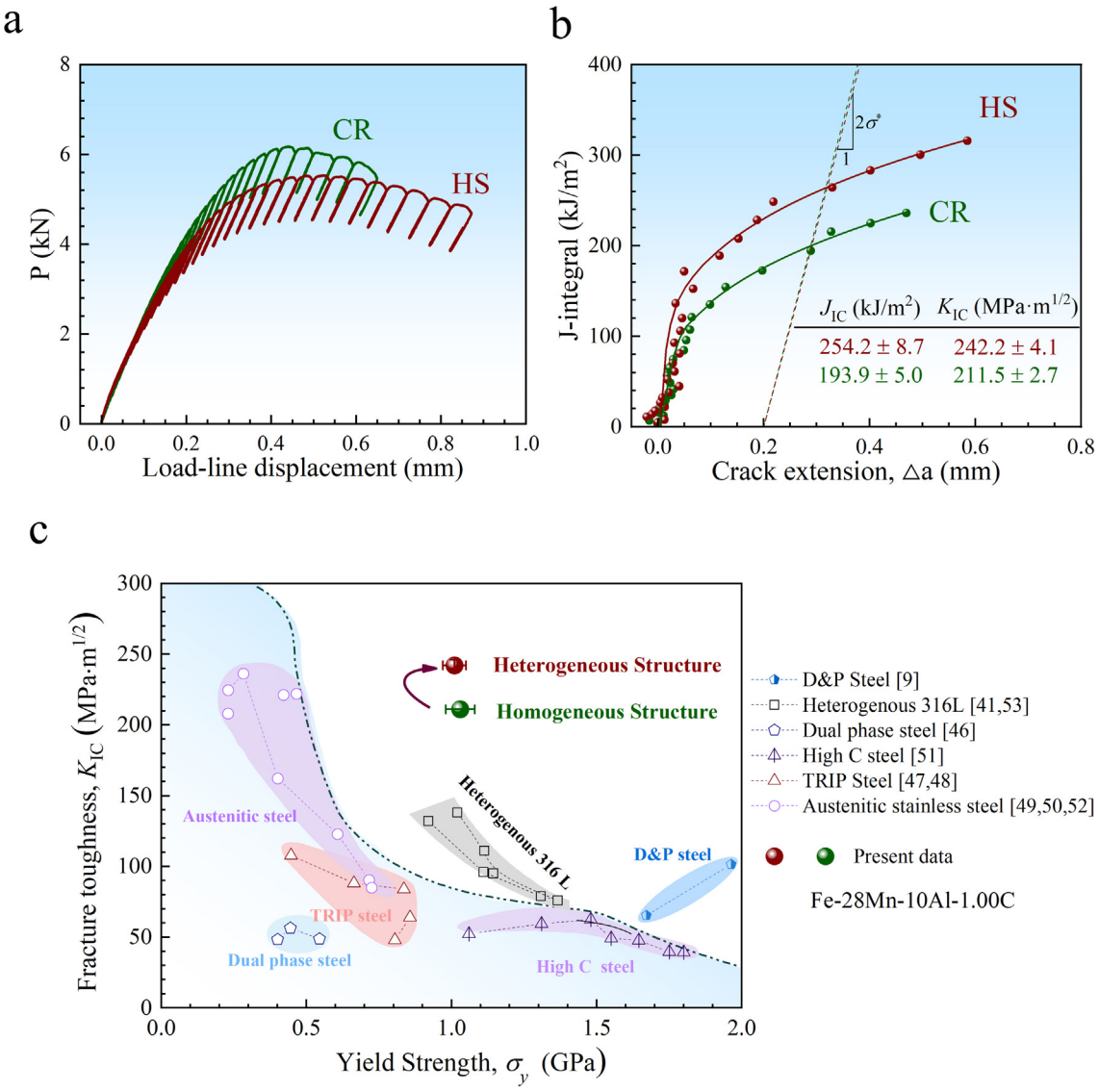

Fig. 4. The curves of fracture toughness tests for the CR sample and the HS sample. (a) Force *P* vs load-line displacement. (b) *J-R* curves. (c) K_{IC} vs σ_y for the present data, along with the data for the other advanced steels [9,41,46–53].

of plastic zone around the crack tips is proportional to the square of intrinsic fracture toughness at a given strength. Thus, the size of plastic zone and the strain hardening capacity around the crack tip for the heterogeneous grain structures are observed to be much larger/higher than those for the homogeneous grain structures at the same level of yield strength, resulting in better fracture toughness in the heterogeneous grain structures.

The detailed EBSD characterizations along the cracks for the HS sample and the CR sample are displayed in Figs. 7 and 8, respectively. The IPF image, the image with various boundaries (high-angle grain boundaries, low-angle grain boundaries and twin boundaries) and the KAM image along the crack path for the HS sample are shown in Fig. 7a1-7a3, the corresponding close-up views for the crack tip area in Fig. 7a1-7a3 are displayed in Fig. 7-b1-7b3. The grain size distribution at the adjacent area of the crack path after fracture test for the HS sample is shown in Fig. 7a4. It is clearly observed that the volume fraction of the small grains increases and the average grain size decreases at the adjacent area of crack path after fracture test for the HS sample. This grain refinement could be due to the high magnitude of the plastic deformation at the adjacent area of the main crack path. Thus the strain hardening from so-called "dynamic H—P effect" [11,12] should be responsible for the high fracture toughness in the HS sample. The histogram distributions of KAM value along the crack path for both UFGs and CGs prior to and after fracture test are shown in Fig. 7b4. It is clearly shown that the average KAM value at the adjacent area of the crack path is much higher than that away from the crack path, is also much higher than that prior to fracture toughness tests (△KAM = 0.92° for UFGs, △KAM = 1.90° for CGs). High density of GNDs can be due to the plastic deformation incompatibility between large grains and small grains, as well as the plastic deformation incompatibility in the grain interiors. It also should be noted that much higher density of low-angle GBs can be observed at the adjacent area of the crack path, which is consistent with the higher KAM value for the adjacent area of the crack path. These observations indicate that high density of GNDs can be induced and numerous low-angle GBs can be formed with the propagation of cracks, resulting in strong strain hardening for high fracture toughness. Moreover, numerous microvoids can also be observed besides the main crack, thus more energy can be dissipated during the crack propagation for higher fracture toughness. These microvoids also confirm that the nucleation and propagation

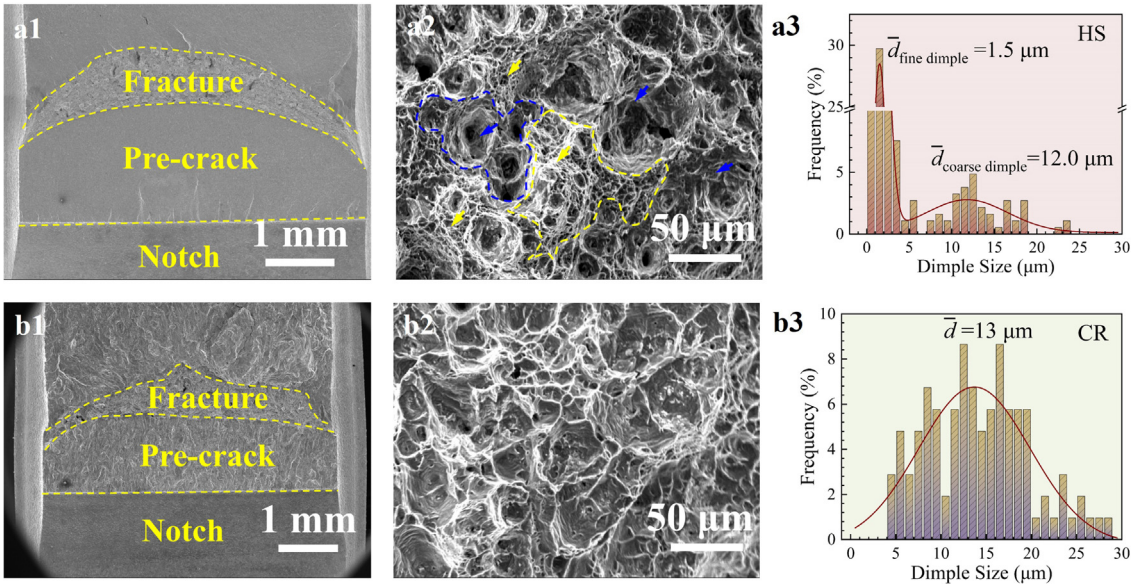

Fig. 5. Fractographies for the HS sample and the CR sample after fracture tests. (a1-a2) SEM observations for the fracture surface of the HS sample. (b1-b2) SEM observations for the fracture surface of the CR sample. The dimple size distributions for (a3) the HS sample and (b3) the CR sample.

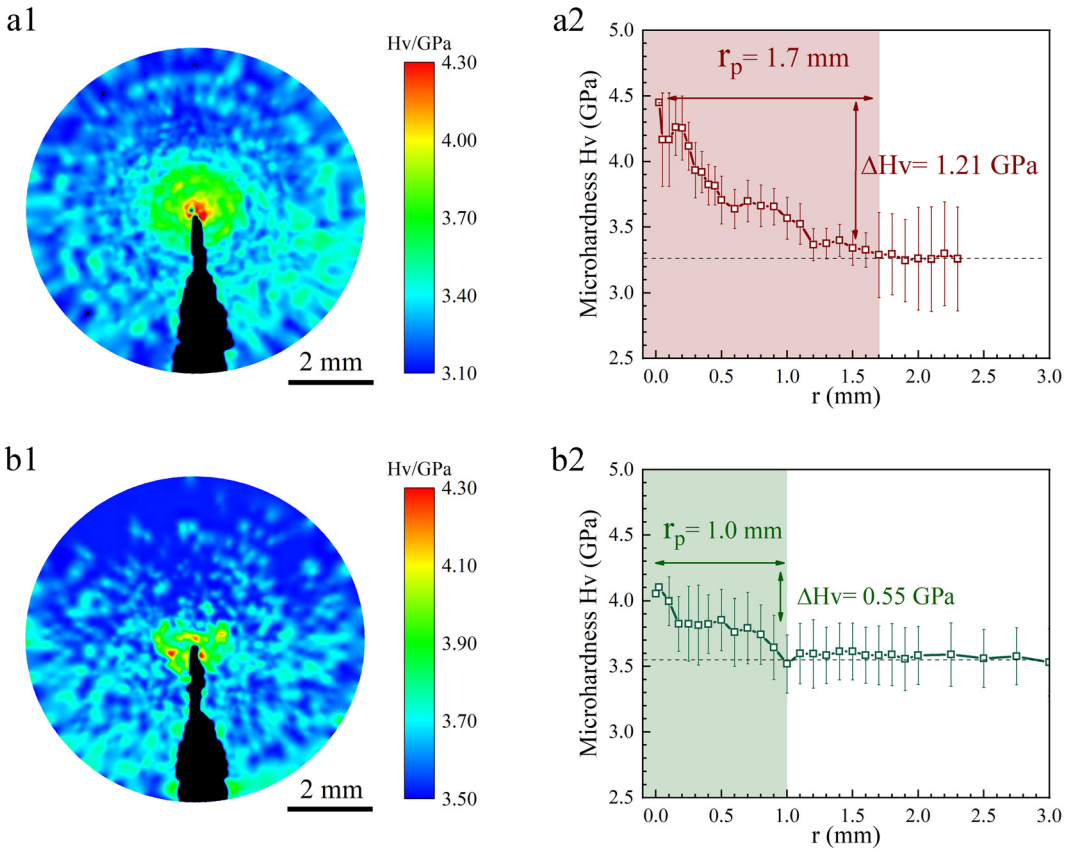

Fig. 6. Contours of the micro-hardness distributions around the crack tips and average micro-hardness values as a function of distance from the crack tips: (a1-a2) for the HS sample; (b1-b2) for the CR sample.

of the main crack are fulfilled by initiation and coalescence of microvoids.

The IPF image, the image with various boundaries (high-angle grain boundaries, low-angle grain boundaries and twin boundaries) and the KAM image along the crack path for the CR sample are displayed in Fig. 8a1-8a3, and the close-up views of IPF images for the crack tip area are shown in Fig. 8b1-8b2. The histogram distributions of KAM value along the crack path for the CR sample prior to and after fracture test are shown in Fig. 8b3. It is clearly indicated that the KAM value is uniformly distributed both at the adjacent area and away from the crack path. Moreover, the average increment of KAM value in Fig. 8b3 is estimated to be 0.82°, which

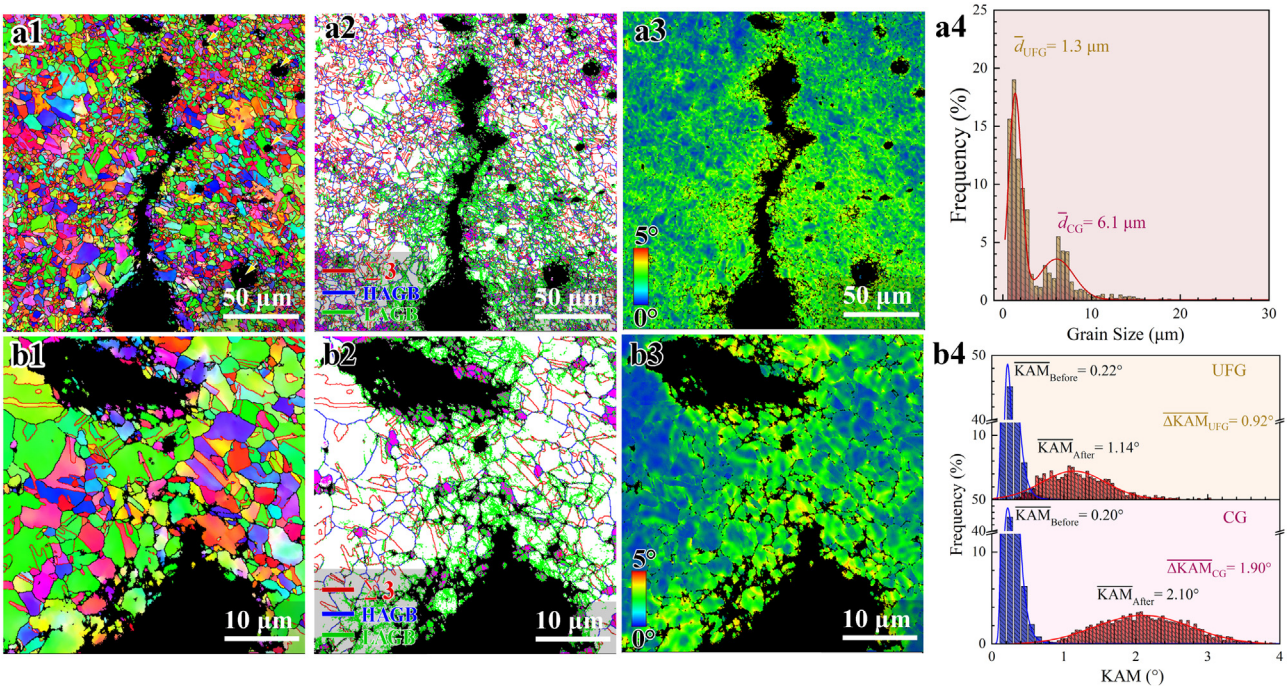

Fig. 7. EBSD characterizations along the crack for the HS sample. (a1) IPF image. (a2) Map with various boundaries. (a3) KAM map. (a4) Grain size distribution at the adjacent area of the crack path after fracture test. (b1-b3) The corresponding close-up views for the crack tip area. (b4) The histogram distributions of KAM value along the crack path for both UFGs and CGs prior to and after fracture test.

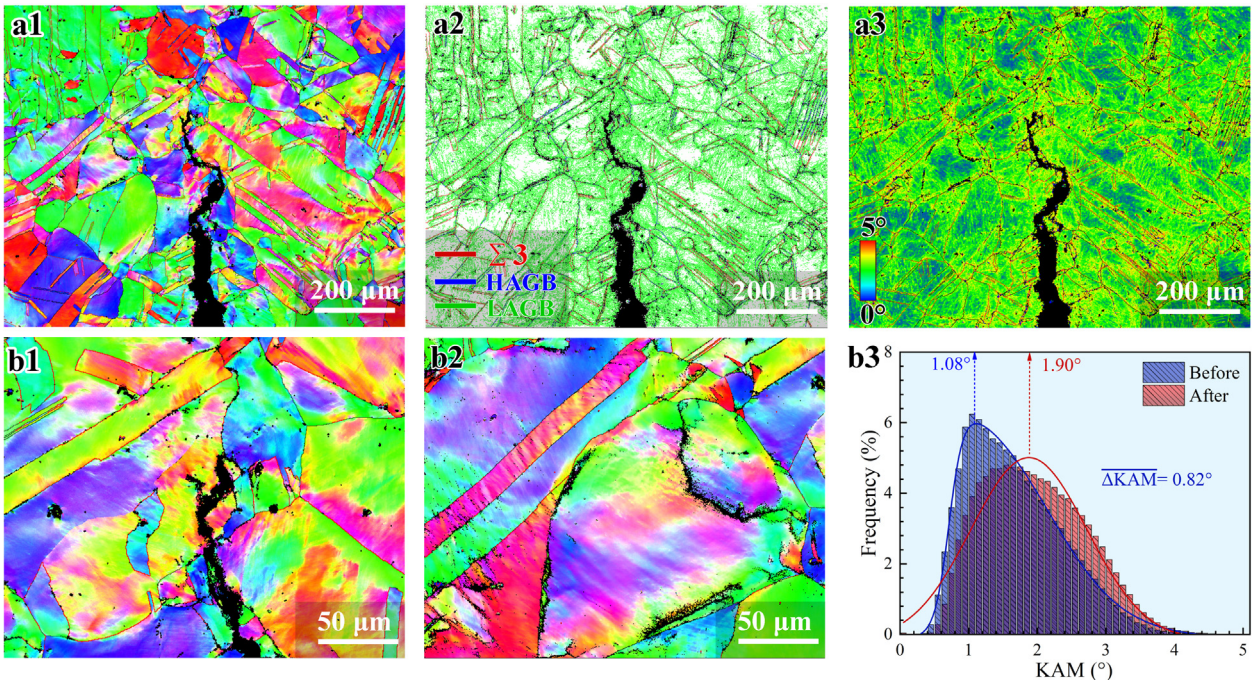

Fig. 8. EBSD characterizations along the crack for the CR sample. (a1) IPF image. (a2) Map with various boundaries. (a3) KAM map. (b1-b2) The corresponding close-up views of IPF images for the crack tip area. (b3) The histogram distributions of KAM value along the crack path prior to and after fracture test.

is much smaller than that for the HS sample. These observations indicate that the plastic deformation is smaller and the strain hardening capacity is lower around the crack path in the CR sample as compared to the HS sample. Moreover, few microvoids are observed besides the main crack, resulting in less energy dissipation during the crack extension. The lower fracture toughness in the CR sample can be attributed to these observations.

TEM characterizations at the adjacent area of the crack tip after fracture tests for the HS sample and the CR sample are displayed in Figs. 9 and 10, respectively. As indicated in Fig. 9c1, 9c2 and 9c3 for the HS sample, the density of dislocations is observed to be very low in both large CG grains and small UFG grains at a distance of 2.0 mm from the crack tip (out of plastic area, r_p = 1.7 mm), which is consistent with the plastic zone size in the Fig. 6a2. At a closer

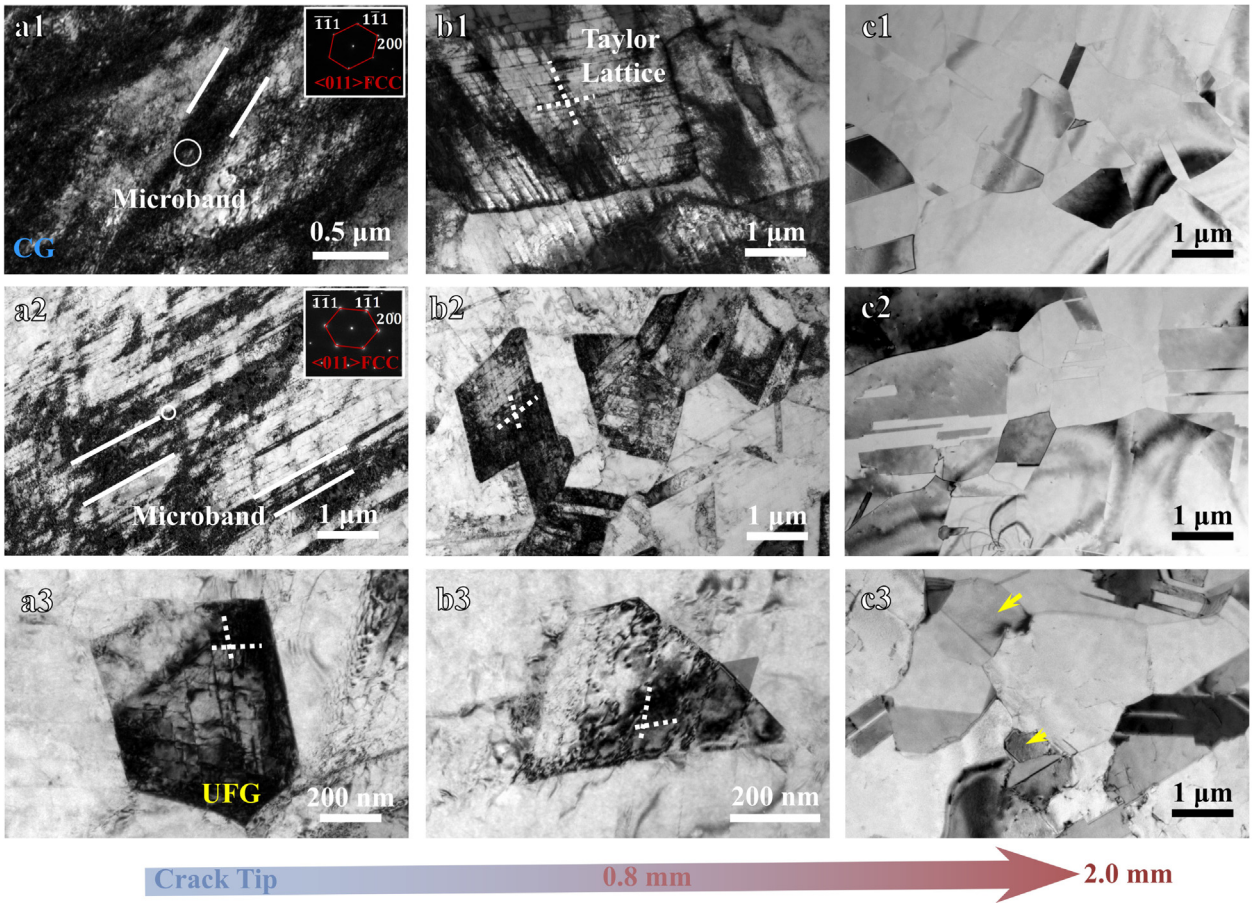

Fig. 9. TEM characterizations at the adjacent area of the crack tip for the HS sample. (a1,a2) At the crack tip for CGs. (b1,b2) With a distance of 0.8 mm from the crack tip for CGs. (c1,c2) With a distance of 2.0 mm from the crack tip for CGs. (a3) At the crack tip for UFGs. (b3) With a distance of 0.8 mm from the crack tip for UFGs. (c3) With a distance of 2.0 mm from the crack tip for UFGs. Dotted lines: slip traces; solid lines: microbands. The insets in a1 and a2 are the selected diffraction patterns for the circled areas.

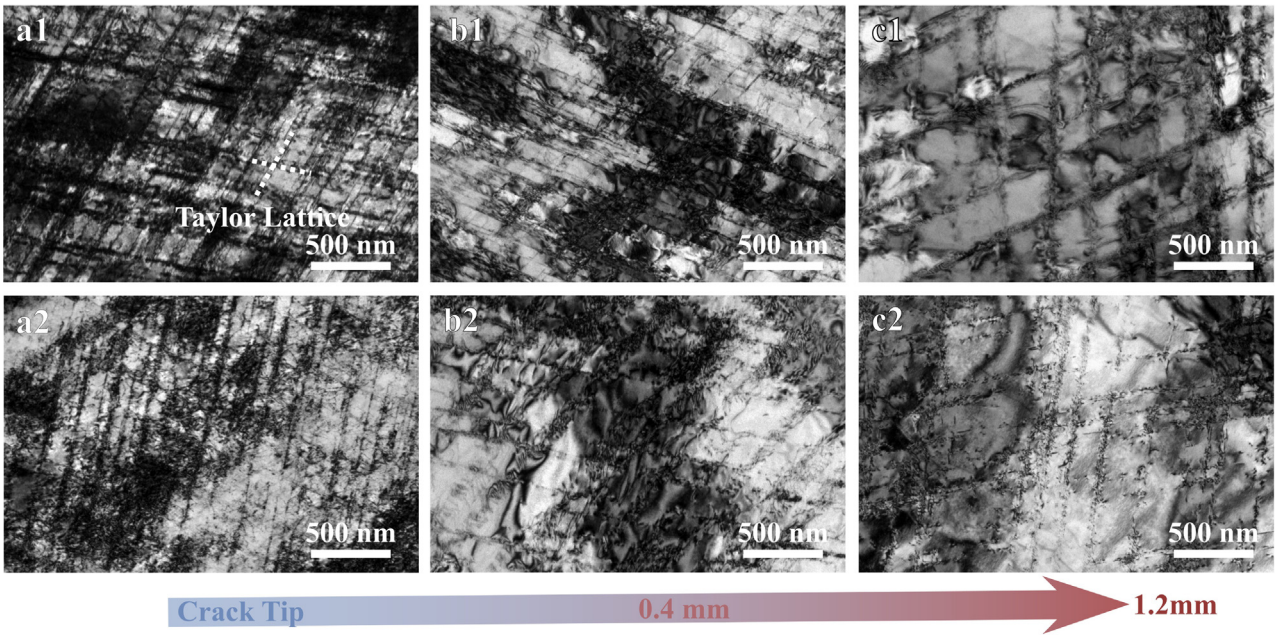

Fig. 10. TEM characterizations at the adjacent area of the crack tip for the CR sample. (a1,a2) At the crack tip. (b1,b2) With a distance of 0.4 mm from the crack tip. (c1,c2) With a distance of 1.2 mm from the crack tip. Dotted lines: slip traces.

distance from the crack tip (0.8 mm, in the plastic area of the crack tip), numerous planar dislocation glides on two {1 1 1} planes are observed in both large CG grains and small UFG grains, and these planar dislocations are found to form Taylor lattices with a relatively low energy (Fig. 9b1, 9b2 and 9b3). The magnitude of the plastic strain is obviously higher at the crack tip, thus single-wall domain boundaries (DBs) form and paired-wall dislocation structures along two directions are observed in the large CG grains, forming microbands (Fig. 9a1 and 9a2). These paralleled microbands divide the grain interior into lots of diamond shaped domains with well-defined boundaries by high density of GNDs. While only Taylor lattices are observed in the small UFG grains at the crack tip (Fig. 9a3). These observations indicate that the formation of microbands is highly dependent on the grain size and requires high magnitude of plastic deformation for the present steel. The formation of microbands can provide strong strain hardening around the crack tip, thus delaying the initiation and propagation of the main crack for high fracture toughness.

It should be recalled that Taylor lattices with a relatively low energy already exist in the CR sample prior to fracture tests (Fig. 2b1 and 2b2). The density of Taylor lattices and the spacing between Taylor lattices at a distance of 1.2 mm from the crack tip (out of plastic area, r_p = 1.0 mm, Fig. 10c1 and 10c2) seem similar to these prior to fracture tests. At a closer distance from the crack tip (0.4 mm, in the plastic area of the crack tip), the density of Taylor lattices becomes higher and the spacing between Taylor lattices is observed to be smaller due to the certain magnitude of plastic strain at this distance (Fig. 10b1 and 10b2). With even higher magnitude of the plastic strain at the crack tip, Taylor lattices become even denser with an extremely smaller interspacing, while no microbands are observed in the CR sample (Fig. 10a1 and 10a2). Thus, the observed higher fracture toughness in the HS sample can be partly attributed to the formation of microbands.

4. Summaries and conclusions

In the present study, heterogeneous grain structures have been designed and fabricated in a high Mn steel. Then the tensile and fracture behaviors, and the corresponding hardening and toughening mechanisms for the heterogeneous grain structures have been studied and compared with those for the homogeneous structures. The new findings are presented as follows:

(1) Larger uniform elongation, stronger strain hardening and higher fracture toughness are observed in the heterogeneous grain structures at the similar yield strength level, as compared to the homogeneous structures. A bimodal dimple size distribution is observed for the heterogeneous grain structures.
(2) The size of plastic zone and the strain hardening capacity around the crack tip are observed to be much larger/higher for the heterogeneous grain structures at the same level of yield strength, as compared to the homogeneous grain structures, resulting in better fracture toughness in the heterogeneous grain structures.
(3) Both grain refinement and high density of geometrically necessary dislocations are observed to be induced at the adjacent area of the main crack path due to the heterogeneous grain size and the high magnitude of plastic deformation, and numerous microvoids are also generated besides the main crack during the crack initiation and propagation for the heterogeneous grain structures, resulting in more energy dissipation for higher fracture toughness.
(4) The microstructure deformation mechanisms at the adjacent area of the crack tip are significantly influenced by the magnitude of plastic strain and the grain size in the HS sample. The formation of microbands can provide strong strain hardening around the crack tip, thus delaying the initiation and propagation of the main crack for the HS sample. The observed higher fracture toughness in the HS sample can be partly attributed to the formation of microbands, which is not observed in the CR sample. The present findings should provide insights on designing heterogeneous microstructures for obtained excellent synergy of strength and toughness in steels.

CRediT authorship contribution statement

Shengde Zhang: Investigation. **Muxin Yang:** Investigation. **Xiaolei Wu:** Conceptualization, Supervision. **Fuping Yuan:** Conceptualization, Writing – original draft, Supervision.

Data availability

Data will be made available on request.

Declaration of Competing Interest

The authors declare that they have no known competing financial interests or personal relationships that could have appeared to influence the work reported in this paper.

Acknowledgements

This research was supported by the NSFC Basic Science Center Program for "Multiscale Problems in Nonlinear Mechanics" [grant number 11988102], the National Key R&D Program of China [grant number 2017YFA0204402], the National Natural Science Foundation of China [grant numbers 52192591 and 11790293].

Data availability statement

The raw/processed data required to reproduce these findings cannot be shared at this time due to technical or time limitations.

References

[1] W.K. Choo, J.H. Kim, J.C. Yoon, Microstructural change in austenitic Fe-30.0wt% Mn-7.8wt%Al-1.3wt%C initiated by spinodal decomposition and its influence on mechanical properties, Acta Mater. 45 (1997) 4877–4885.
[2] M. Militzer, A synchrotron look at steel, Science 298 (2002) 975–976.
[3] G. Frommeyer, U. Bruex, Microstructures and mechanical properties of high strength Fe-Mn-Al-C light-weight TRIPLEX steels, Steel Res. Int. 77 (2006) 627–633.
[4] S. Chen, R. Rana, A. Haldar, R.K. Ray, Current state of Fe-Mn-Al-C low density steels, Prog. Mater. Sci. 89 (2017) 345–391.
[5] B.B. He, B. Hu, H.W. Yen, G.J. Cheng, Z.K. Wang, H.W. Luo, M.X. Huang, High dislocation density-induced large ductility in deformed and partitioned steels, Science 357 (2017) 1029–1032.
[6] M.J. Yao, E. Welsch, D. Ponge, S.M.H. Haghighat, S. Sandlobes, P. Choi, M. Herbig, I. Bleskov, T. Hickel, M. Lipinska-Chwalek, P. Shanthraj, C. Scheu, S. Zaefferer, B. Gault, D. Raabe, Strengthening and strain hardening mechanisms in a precipitation-hardened high-Mn lightweight steel, Acta Mater. 140 (2017) 258–273.
[7] S.H. Jiang, H. Wang, Y. Wu, X.J. Liu, H.H. Chen, M.J. Yao, B. Gault, D. Ponge, D. Raabe, A. Hirata, M.W. Chen, Y.D. Wang, Z.P. Lu, Ultrastrong steel via minimal lattice misfit high density nanoprecipitation, Nature 544 (2017) 460–464.
[8] Z.W. Wang, W.J. Lu, H. Zhao, C.H. Liebscher, J.Y. He, D. Ponge, D. Raabe, Z.M. Li, Ultrastrong lightweight compositionally complex steels via dual-nanoprecipitation, Sci. Adv. 6 (2020) eaba9543.
[9] L. Liu, Q. Yu, Z. Wang, J. Ell, M.X. Huang, R.O. Ritchie, Making ultrastrong steel tough by grain-boundary delamination, Science 368 (2020) 1347–1352.
[10] B. Gao, Q.Q. Li, Y. Cao, R. Hu, L.R. Xiao, Z.Y. Pan, N.N. Liang, Y.S. Li, G. Sha, M.P. Liu, H. Zhao, X.L. Wu, Y.T. Zhu, Ultrastrong low-carbon nanosteel produced by heterostructure and interstitial mediated warm rolling, Sci. Adv. 6 (2020) eaba8169.
[11] O. Bouaziz, S. Allain, C.P. Scott, P. Cugy, D. Barbier, High manganese austenitic twinning induced plasticity steels: a review of the microstructure properties relationships, Curr. Opin. Solid St. Mater. Sci. 15 (2011) 141–168.

[12] B.C. De Cooman, Y. Estrin, S.K. Kim, Twinning-induced plasticity (TWIP) steels, Acta Mater. 142 (2018) 283–362.
[13] V. Atreya, J.S. Van Dokkum, C. Bos, M.J. Santofimia, Effect of the anisotropy of martensitic transformation on ferrite deformation in Dual-Phase steels, Mater. Des. 219 (2022) 110805.
[14] M. Calcagnotto, Y. Adachi, D. Ponge, D. Raabe, Deformation and fracture mechanisms in fine- and ultrafine-grained ferrite/martensite dual-phase steels and the effect of aging, Acta Mater. 59 (2011) 658–670.
[15] P. Xie, M. Han, C.L. Wu, Y.Q. Yin, K. Zhu, R.H. Shen, J.H. Chen, A high-performance TRIP steel enhanced by ultrafine grains and hardening precipitates, Mater. Des. 127 (2017) 1–7.
[16] F.D. Fischer, G. Reisner, E. Werner, A new review on transformation induced plasticity (TRIP), Inter. J. Plast. 16 (2000) 723–748.
[17] J.D. Yoo, K.-T. Park, Microband-induced plasticity in a high Mn-Al-C light steel, Mater. Sci. Eng. A 496 (2008) 417–424.
[18] J.D. Yoo, S.W. Hwang, K.-T. Park, Factors influencing the tensile behavior of a Fe-28Mn-9Al-0.8C steel, Mater. Sci. Eng. A 508 (2009) 234–240.
[19] I. Gutierrez-Urrutia, D. Raabe, Microbanding mechanism in an Fe-Mn-C high-Mn twinning-induced plasticity steel, Scr. Mater. 69 (2013) 53–56.
[20] I. Gutierrez-Urrutia, D. Raabe, Influence of Al content and precipitation state on the mechanical behavior of austenitic high-Mn low-density steels, Scr. Mater. 68 (2013) 343–347.
[21] J. Moon, S.-J. Park, C. Lee, H.N. Han, T.-H. Lee, C.-H. Lee, Microstructure evolution and age-hardening behavior of microalloyed austenitic Fe-30Mn-9Al-0.9C light-weight steels, Metall. Mater. Trans. A 48A (2017) 4500–4510.
[22] J. Xing, Y.H. Wei, L.F. Hou, An overview of the effects of alloying elements on the properties of lightweight Fe-(15–35) Mn-(5–12) Al-(0.3-1.2) C steel, JOM 70 (2018) 929–937.
[23] J. Moon, S.-J. Park, J.H. Jang, T.-H. Lee, C.-H. Lee, H.-U. Hong, H.N. Han, J. Lee, B. H. Lee, C. Lee, Investigations of the microstructure evolution and tensile deformation behavior of austenitic Fe-Mn-Al-C lightweight steels and the effect of Mo addition, Acta Mater. 147 (2018) 226–235.
[24] S.D. Zhang, Y.K. Liu, J. Wang, S. Qin, X.L. Wu, F.P. Yuan, Tensile behaviors and strain hardening mechanisms in a high-Mn steel with heterogeneous microstructure, Materials 15 (2022) 3542.
[25] W. Wang, Y.K. Liu, Z.H. Zhang, M.X. Yang, L.L. Zhou, J. Wang, P. Jiang, F.P. Yuan, X.L. Wu, Deformation mechanisms for a new medium-Mn steel with 1.1 GPa yield strength and 50% uniform elongation, J. Mater. Sci. Tech. 132 (2023) 110–118.
[26] F. Yang, R. Song, Y. Li, T. Sun, K. Wang, Tensile deformation of low density duplex Fe–Mn–Al–C steel, Mater. Des. 76 (2015) 32–39.
[27] J. Zhang, C. Hu, Y. Zhang, J. Li, C. Song, Q. Zhai, Microstructures, mechanical properties and deformation of near-rapidly solidified low-density Fe-20Mn-9Al-1.2C-xCr steels, Mater. Des. 186 (2020) 108307.
[28] M.S. Rizi, H. Minouei, B.J. Lee, M.R. Toroghinejad, S.I. Hong, Effects of carbon and molybdenum on the nanostructural evolution and strength/ductility trade-off in Fe40Mn40Co10Cr10 high-entropy alloys, J. Alloys Compd. 911 (2022) 165108.
[29] M.S. Rizi, H. Minouei, B.J. Lee, H. Pouraliakbar, M.R. Toroghinejad, S.I. Hong, Hierarchically activated deformation mechanisms to form ultra-fine grain microstructure in carbon containing FeMnCoCr twinning induced plasticity high entropy alloy, Mater. Sci. Eng. A 824 (2021) 141803.
[30] Y.M. Wang, M.W. Chen, F.H. Zhou, E. Ma, High tensile ductility in a nanostructured metal, Nature 419 (2002) 912–915.
[31] Y.H. Zhao, T. Topping, J.F. Bingert, J.J. Thornton, A.M. Dangelewicz, Y. Li, W. Liu, Y.T. Zhu, Y.Z. Zhou, E.L. Lavernia, High tensile ductility and strength in bulk nanostructured nickel, Adv. Mater. 20 (2008) 3028–3033.
[32] D.B. Santos, A.A. Saleh, A.A. Gazder, A. Carman, D.M. Duarte, É.A.S. Ribeiro, B.M. Gonzalez, E.V. Pereloma, Effect of annealing on the microstructure and mechanical properties of cold rolled Fe-24Mn-3Al-2Si-1Ni-0.06C TWIP steel, Mater. Sci. Eng. A 528 (2011) 3545–3555.
[33] Y.T. Zhu, X.L. Wu, Perspective on hetero-deformation induced (HDI) hardening and back stress, Mater. Res. Lett. 7 (2019) 393–398.
[34] M.E. Launey, R.O. Ritchie, On the fracture toughness of advanced materials, Adv. Mater. 21 (2009) 2103–2110.
[35] E.W. Qin, L. Lu, N.R. Tao, J. Tan, K. Lu, Enhanced fracture toughness and strength in bulk nanocrystalline Cu with nanoscale twin bundles, Acta Mater. 57 (2009) 6215–6225.
[36] R.O. Ritchie, The conflicts between strength and toughness, Nature Mater. 10 (2011) 817–822.
[37] B. Gludovatz, A. Hohenwarter, D. Catoor, E.H. Chang, E.P. George, R.O. Ritchie, A fracture-resistant high-entropy alloy for cryogenic applications, Science 345 (2014) 1153–1158.
[38] R. Pippan, A. Hohenwarter, The importance of fracture toughness in ultrafine and nanocrystalline bulk materials, Mater. Res. Lett. 4 (2016) 127–136.
[39] B. Gludovatz, A. Hohenwarter, K.V. Thurston, H. Bei, Z. Wu, E.P. George, R.O. Ritchie, Exceptional damage-tolerance of a medium-entropy alloy CrCoNi at cryogenic temperatures, Nat. commun. 7 (2016) 10602.
[40] H.F. Li, S.G. Wang, P. Zhang, R.T. Qu, Z.F. Zhang, Crack propagation mechanisms of AISI 4340 steels with different strength and toughness, Mater. Sci. Eng. A 729 (2018) 130–140.
[41] L. Xiong, Z.S. You, S.D. Qu, L. Lu, Fracture behavior of heterogeneous nanostructured 316L austenitic stainless steel with nanotwin bundles, Acta Mater. 150 (2018) 130–138.
[42] R.Q. Cao, Q. Yu, J. Pan, Y. Lin, A. Sweet, Y. Li, R.O. Ritchie, On the exceptional damage-tolerance of gradient metallic materials, Mater. Today 32 (2020) 94–107.
[43] Y. Lin, Q. Yu, J. Pan, F.H. Duan, R.O. Ritchie, Y. Li, On the impact toughness of gradient-structured metals, Acta Mater. 193 (2020) 125–137.
[44] S.D. Zhang, M.X. Yang, F.P. Yuan, L.L. Zhou, X.L. Wu, Extraordinary fracture toughness in nickel induced by heterogeneous grain structure, Mater. Sci. Eng. A 830 (2022) 142313.
[45] ASTM E1820-15, Standard Test Method for Measurement of Fracture Toughness, ASTM International, West Conshohocken, PA, 2015, www.astm.org.
[46] A. Bayram, A. Uguz, M. Ula, Effects of microstructure and notches on the mechanical properties of dual-phase steels, Mater. Charact. 43 (1999) 259–269.
[47] R. Eckner, L. Krüger, C. Ullrich, M. Wendler, O. Volkova, Fracture toughness of high-alloy austenitic-martensitic TRIP steels after Q&P processing, Int. J. Fract. 215 (2018) 139–151.
[48] J. Kobayashi, D. Ina, A. Futamura, K.-I. Sugimoto, Fracture Toughness of an Advanced Ultrahigh-strength TRIP-aided Steel, ISIJ Int. 54 (2014) 955–962.
[49] W.J. Mills, Fracture toughness of type 304 and 316 stainless steels and their welds, Int. Mater. Rev. 42 (2013) 45–82.
[50] J.E. Pawel, D.J. Alexander, M.L. Grossbeck, A.W. Longest, A.F. Rowcliffe, G.E. Lucas, S. Jitsukawa, A. Hishinuma, K. Shiba, Fracture toughness of candidate materials for ITER first wall, blanket, and shield structures, J. Nucl. Mater. 212–215 (1994) 442–447.
[51] S.K. Putatunda, Fracture toughness of a high carbon and high silicon steel, Mater. Sci. Eng. A 297 (2001) 31–43.
[52] G. Sasikala, S.K. Ray, Influence of ageing on the quasistatic fracture toughness of an SS 316(N) weld at ambient and elevated temperatures, J. Nucl. Mater. 408 (2011) 45–53.
[53] L. Xiong, Z.S. You, L. Lu, Enhancing fracture toughness of nanotwinned austenitic steel by thermal annealing, Scr. Mater. 119 (2016) 55–59.